Spectrochimica Acta Part B 94–95 (2014) 39–47

Contents lists available at ScienceDirect

Spectrochimica Acta Part B

journal homepage: www.elsevier.com/locate/sab

Liquid sampling-atmospheric pressure glow discharge as a secondary excitation source: Assessment of plasma characteristics

Benjamin T. Manard [a,b], Jhanis J. Gonzalez [b], Arnab Sarkar [b,c], Meirong Dong [b], Jose Chirinos [b], Xianglei Mao [b], Richard E. Russo [b,*], R. Kenneth Marcus [a]

[a] Department of Chemistry, Clemson University, Clemson, SC 29634, USA
[b] Lawrence Berkeley National Laboratory, Berkeley, CA 94720, USA
[c] Fuel Chemistry Division, Bhabha Atomic Research Centre, Mumbai 400085, India

ARTICLE INFO

Article history:
Received 15 October 2013
Accepted 6 March 2014
Available online 21 March 2014

Keywords:
LS-APGD
Laser ablation
Liquid sampling-atmospheric pressure glow discharge

ABSTRACT

The liquid sampling-atmospheric pressure glow discharge (LS-APGD) has been assessed as a secondary excitation source with a parametric evaluation regarding carrier gas flow rate, applied current, and electrode distance. With this parametric evaluation, plasma optical emission was monitored in order to obtain a fundamental understanding with regards to rotational temperature (T_{rot}), excitation temperature (T_{exc}), electron number density (n_e), and plasma robustness. Incentive for these studies is not only for a greater overall fundamental knowledge of the APGD, but also in instrumenting a secondary excitation/ionization source following laser ablation (LA). Rotational temperatures were determined through experimentally fitting of the N_2 and OH molecular emission bands while atomic excitation temperatures were calculated using a Boltzmann distribution of He and Mg atomic lines. The rotational and excitation temperatures were determined to be ~1000 K and ~2700 K respectively. Electron number density was calculated to be on the order of $\sim 3 \times 10^{15}$ cm^{-3} utilizing Stark broadening effects of the Hα line of the Balmer series and a He I transition. In addition, those diagnostics were performed introducing magnesium (by solution feed and laser ablation) into the plasma in order to determine any perturbation under heavy matrix sampling. The so-called plasma robustness factor, derived by monitoring Mg II/Mg I emission ratios, is also employed as a reflection of potential perturbations in microplasma energetics across the various operation conditions and sample loadings. While truly a miniaturized source (<1 mm^3 volume), the LS-APGD is shown to be quite robust with plasma characteristics and temperatures being unaffected upon introduction of metal species, whether by liquid or laser ablation sample introduction.

1. Introduction

As the trend of miniaturization in analytical chemistry instrumentation has progressed, the development of new atmospheric pressure plasma sources has seen increased interest. Currently, there is a need to design spectrochemical instruments with lower power consumption, reduced sample sizes, compact footprint, low operating costs, and the ability to be operated under ambient conditions [1–3]. Reductions in sampling size have been addressed over the past two decades by laser-ablation (LA), allowing for chemical analysis of solids without sample preparation [4–6]. LA utilizes a short-pulsed, high-power laser beam to remove material for either a direct analysis of the plasma volume by optical emission spectroscopy (OES) or to be transported into a secondary excitation/ionization source such as the inductively coupled plasma (ICP) [7,8]. The former, termed laser-induced breakdown spectroscopy (LIBS), is easily miniaturized for portability with applications expanding to exploration on the surface of Mars [9,10]. By utilizing a secondary source, higher power densities and longer residence times can be utilized for enhanced sensitivity and lower limits of detection (LODs) when compared to LIBS [6,11]. To this end, atto-/femtogram detections limits are readily achieved in ICP-MS [12].

Unfortunately, the conventional ICP is not ideal as a secondary source as minute amounts of ablated mass are introduced into the relatively large plasma volume (~125 mm^3), not to mention the high operating cost and large footprint of the base ICP-OES/MS instrument [6]. Few efforts have addressed miniaturizing the ICP or reducing the operational overhead of LA-ICP instrumentation. Improving designs by incorporating alternative plasmas as the secondary excitation/ionization source of particulates should be explored, especially regarding the miniaturization of the spectrochemical instrumentation. In recent years, a few secondary sources have been proposed for the detection of laser ablated particles such as microwave induced plasmas (MIP) and the flowing atmospheric pressure afterglow (FAPA) [4,13].

Marcus and co-workers developed a liquid sampling-atmospheric pressure glow discharge (LS-APGD), which is sustained between an

* Corresponding author.

http://dx.doi.org/10.1016/j.sab.2014.03.004
0584-8547/

electrolytic liquid (HNO_3) flowing from a glass capillary and a metallic counter electrode placed ~2 mm away [14–16]. The operational space of this excitation/ionization source fits well in terms of the miniaturization characteristics mentioned above. While early LS-APGD works focused on OES monitoring, recent efforts have demonstrated the ability of the source to effectively ionize solution-introduced species by mass spectrometry (MS) [17,18]. The scope of application has been expanded through the introduction of LA-generated particles [19,20]. This combination, LA-LS-APGD, has been shown to be qualitatively similar to LA-ICP, with efficient vaporization/excitation/ionization of particles produced from nanosecond and femtosecond pulsed lasers. Particularly relevant for LA sampling, the LS-APGD operates at much higher power densities (~10 W mm^{-3} versus 0.1 W mm^{-3}) and a much smaller plasma volume (~1 mm^3 versus ~125 mm^3) than the ICP (i.e., less dilution). Finally, simple gas dynamics calculations suggest plasma transit times of 5–30 ms vs. ~1 ms for the ICP, though these must be verified experimentally.

When assessing plasma performance, fundamental properties must be characterized to understand excitation conditions, which may vary with operation parameters or the introduction of sample material [21,22]. Optical emission spectroscopy (OES) is a versatile means of characterization of atmospheric pressure flames and plasmas, typically by the fitting of molecular bands (e.g., N_2, OH) to obtain rotational temperatures (T_{rot}), determinations of excitation temperatures (T_{exc}) by monitoring excited states of various species such as plasma gases or sample species, and measurement of the broadening of emission lines (H, He) to yield plasma electron number densities (n_e) [23–25]. Finally, the ability of an spectrochemical source to be immune to sample-induced perturbations can be assessed through changes in the "robustness" factor determined by the Mg II/Mg I emission intensity ratios [26,27].

The research presented here utilizes OES to evaluate the properties of the LS-APGD to gain fundamental knowledge regarding the source as a means for secondary excitation/ionization of LA-introduced particles. T_{rot}, T_{exc}, and n_e were evaluated across a matrix of plasma operation conditions generated through a central composite, design of experiments (DOE) approach, studying the roles of electrode separation distance, discharge current, and carrier gas (He) flow rate. Molecular bands, OH and the N_2 second positive system [28] were utilized for rotational/vibrational temperatures while the emission of He and Mg lines was utilized for the determination of excitation temperatures and plasma robustness. In addition to baseline values for these quantities determined for aqueous HNO_3 blanks, the plasma was stressed by introduction of large amounts of magnesium, to determine potential deleterious effects due to sample matrix. In one case, Mg^{2+} was added in the nitric acid feed at a concentration of 1000 μg mL^{-1}, and in the other case metal shards were compacted in a paraffin matrix and introduced via laser ablation. Such studies set the stage for applications in the analysis of matrix-laden solutions and LA sampling.

2. Materials and methods

2.1. LS-APGD source

The LS-APGD source is relatively unchanged from previous publications, incorporating the flow of laser-ablated particles into the microplasma through the *hollow* counter electrode [19,20]. The microplasma is sustained between an electrolytic solution (5% HNO_3) and the counter electrode (nickel, 0.3 cm o.d., 0.1 cm i.d.) through which the He carrier gas flows, transporting ablated particles from the ablation cell into the plasma volume. A syringe pump (New Era Pump Systems Inc., model NE-1000 Multi-Phaser, Farmingdale, NY) was used to deliver the electrolytic solution through a fused silica capillary (360 μm o.d., 100 μm i.d. Idex Health and Science, Oak Harbor, WA) which is housed within a metal capillary (nickel, 0.16 cm o.d., 0.06 cm i.d.). Helium was employed as a sheath gas (0.2 L min^{-1}) flowing between the capillaries, as optimized in a previous publication [19]. Power for the microplasma was delivered by a Glassman High Voltage Inc. power supply (0–100 mA, 0–2 kV, High Bridge, NJ) operating positive polarity with a 10 kΩ, 225 W ballast resistor (Ohmite, Arlington Heights, IL) placed in-line with the powered solution electrode (the counter electrode was held at ground potential). It is important to point out that the entirety of the LS-APGD plasma components, power supply, gas metering, and the ablating laser are mounted on a single 30.5 × 30.5 cm^2 optical bread board. Potential plasma perturbations were assessed by introducing 1000 μg mL^{-1} magnesium (CPI International, Santa Rosa, CA) in the electrolytic feed solution and by the ablation of a 2% Mg pellet (2% in paraffin) that was made in-house (LBNL).

2.2. Laser ablation apparatus

For the introduction of laser ablated particles a commercial laser ablation system (J100 Applied Spectra, Inc., Freemont, CA, USA) consisting of a nanosecond laser (Nd:YAG) with a 5-ns pulse duration was used and operated at its fundamental wavelength of 1064 nm, and variable energy (max 50 mJ) and repetition rate (1–10 Hz). Laser ablation was performed in a helium atmosphere. The J-100 ablation system is equipped with an ablation chamber that could accommodate samples up to 100 mm diameter with flexibility in volume and wash-out time.

2.3. Optical emission measurements

Broad wavelength range measurements were performed using an optical fiber-based spectrometer (Aurora, Applied Spectra, Fremont, CA). This spectrometer consists of six channels, each composed of a 2048 pixel CCD detector dedicated to different spectra regions. A fused silica biconvex lens (35 mm focal length, 25.4 mm diameter) was used to focus the entire microplasma image onto the input optic of the fiber bundle connected to the spectrometer. While there are known inhomogeneities in the LS-APGD [29], this approach is the most pragmatic way of sampling the ~1 mm^3 plasma volume, analogous to the case with LIBS analyses. A composite (simultaneous) spectrum is acquired using a 1.05 ms gate over each of the 500 laser shots, with spectral resolution of 0.05–0.12 nm across the 190–1040 nm wavelength range. For the calculation of n_e, Stark broadening of the H (I) 656.3 nm and He (I) 587.6 nm lines was measured employing a 1.25 m focal length, 2400 gr mm^{-1} grating, Czerny–Turner spectrometer (Horiba-JY, Model 1250 M, Longjumeau, France), with an intensified charged-coupled device (ICCD) detector (Princeton Instruments, PI MAX 1024 Gen II, Trenton, NJ 08619, USA). This detection system yields a spectral window of ~13 nm with 0.04 nm resolution. The same optical coupling was used in this case as the analytical (array) spectrometer system. Experimentally-determined line widths were processed under Lorenz fitting to isolate Stark effects from Doppler broadening contributions. Corrections were employed by subtracting the FWHM from the corresponding Hg lines to correct for instrument broadening [30]. The ICCD acquisition was set at a 1 μs delay, a gate width of 150 μs, and a gain set at 200 out of a maximum setting of 256. Due to experimental constraints, laser ablation sample introduction could not be performed in conjunction with the high-resolution optical measurements.

2.4. Experimental design

The various plasma species were optically monitored during the course of varying the electrode gap, He carrier gas flow rate, and applied current of the LS-APGD, with the specific parameters listed in Table 1. A central composite DOE, with three experimental factors, was used to study the effects of the operating parameters on the plasma properties [31]. The experimental design and the surface responses were generated using Statgraphics (Warrenton, VA). The central composite design generates a random sequence of experiments and parameter combinations across a range of parameter values centered among typical operating conditions. A total of n = 16 parameter combinations was

Table 1
LS-APGD microplasma operation parameters employed throughout this work.

Parameter	Range	Step
Current (mA)	45–65	5
Carrier gas (He) flow rate (L min^{-1})	0.15–0.75	0.2
Electrode gap (mm)	0.5–3.5	0.5
Solution flow rate (μL $min^{-1)}$	300	Constant
Sheath gas (He) flow rate (L min^{-1})	0.2	Constant

used throughout this work; chosen by the algorithm. In each set of plasma characteristic determinations, estimated response surfaces are generated to illustrate cooperative effects of two parameters, keeping the third constant. The determined values (i.e. plasma temperatures, etc.) were processed using a multiple linear regression approach to determine the significance of parameter effects. The analysis is presented in the form of standard Pareto plots [32], indicating the magnitude of each parametric dependency (including cross dependencies) and their statistical significance relative to the overall experimental variability. A statistical significance value of 2.57 was used here (as designated by the vertical line on each plot), based on the 5 degrees of experimental freedom and a 95% confidence level. Throughout this work, the electrode gap is indicated as parameter A, the He carrier gas flow rate B, and the discharge current C, with the cross-dependencies indicated as the products of those letters.

3. Results and discussion

3.1. Spectroscopic characteristics and identification of species in the LS-APGD

Optical emission spectroscopy (OES) is an excellent tool for performing plasma diagnostics. In the case of the LS-APGD, the various probe species enter the plasma from the electrolytic solution, the sheath/carrier gas (He), and as ambient species. The spectral breadth of the spectrometer (190–1040 nm) allows for comprehensive sampling in a simultaneous fashion. Fig. 1 shows a broadband spectrum collected from LS-APGD with the simple introduction of the plasma-sustaining electrolytic HNO_3 solution. Molecular bands such as OH and N_2 are present and are used to provide rotational temperatures (T_{rot}). OH molecular emission ($A^2\sum^+ \rightarrow X^2\prod$) can be seen from 306 nm extending to ~316 nm where an interference exists from N_2 band structure. The N_2 second positive molecular system ($c^3\prod_u \rightarrow B^3\prod_g$) is seen as prominent bands across the range of 316 nm to 405 nm. There also is strong emission from atomic species including H I, He I, O I, and N I. The hydrogen Balmer lines (H_α (656.3 nm) and H_β (486.1 nm)) and He I lines at 587.6 and 706.5 nm are routinely employed for the determination of electron number density (n_e) through Stark broadening. Beyond these features, the spectra of analytes introduced into the plasma are dominated by atomic transitions, more in line with those of flame spectroscopy [23] rather than the ionic transitions common to ICP sources [33]. This spectral simplicity improves the potential for development of portable instrumentation using compact, array-based spectrometers.

3.2. Determination of rotational temperatures by N_2 and OH molecular bands

Plasma rotational temperatures were investigated in order to understand how each parameter affected the kinetic energy input. Rotational temperatures are important when characterizing plasmas due to the assumption that T_{rot} is the same magnitude as gas-kinetic temperatures, implied from lower energies involved in the excitation process and the rapid interchange between the rotational and kinetic energy of a molecule [34,35]. The fitting of experimental emission spectra for the determination of rotational and vibrational temperatures is frequently employed [36], as demonstrated for LIBS analysis [10,37]. The calculations, simulation information, and band fitting parameters utilized in these studies are expressed thoroughly with a detailed design in those publications [10,37,38]. The spectra were fit to the $\Delta v = -1$ and $\Delta v = -2$ bands for N_2 as seen in Fig. 2a for each experimental condition ($n = 16$). The average T_{rot} across all conditions was determined to be 831 for the fitting of the $\Delta v = -1$, and 742 K for each condition for the $\Delta v = -2$ bands; ranging from 730 to 1100 K over the totality of parameters. Importantly, the values obtained at any one set of conditions is reproducible to better than 1% RSD.

Fig. 3a depicts a typical N_2-based T_{rot} response surface generated through the central composite DOE parameters, changing the He carrier gas flow rate and the discharge current, and holding the electrode spacing constant. Statistical analysis of the interrelated (standardized)

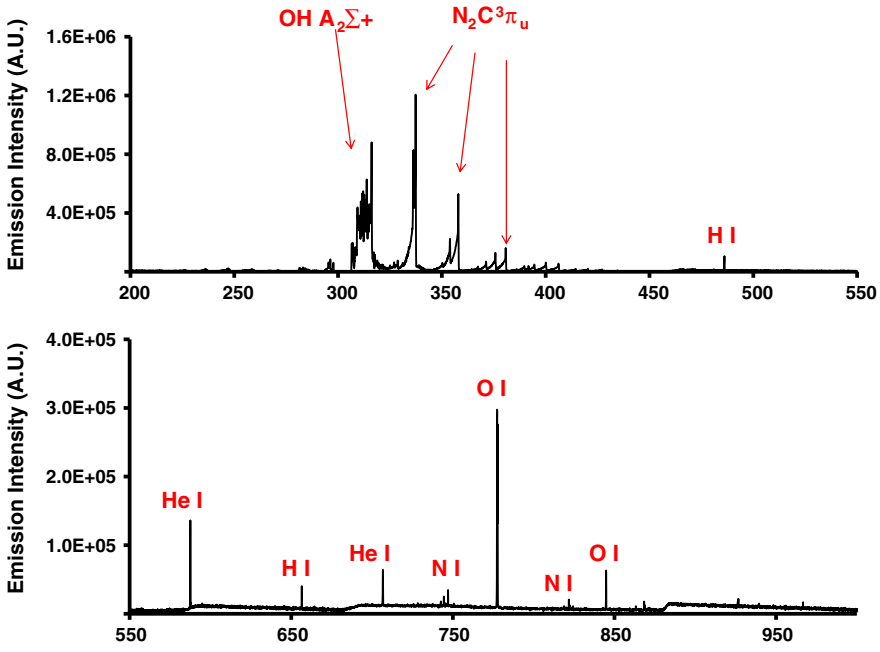

Fig. 1. Broadband spectra (190–1010 nm) collected from Aurora Spectrometer illustrating the presence of molecular and atomic species.

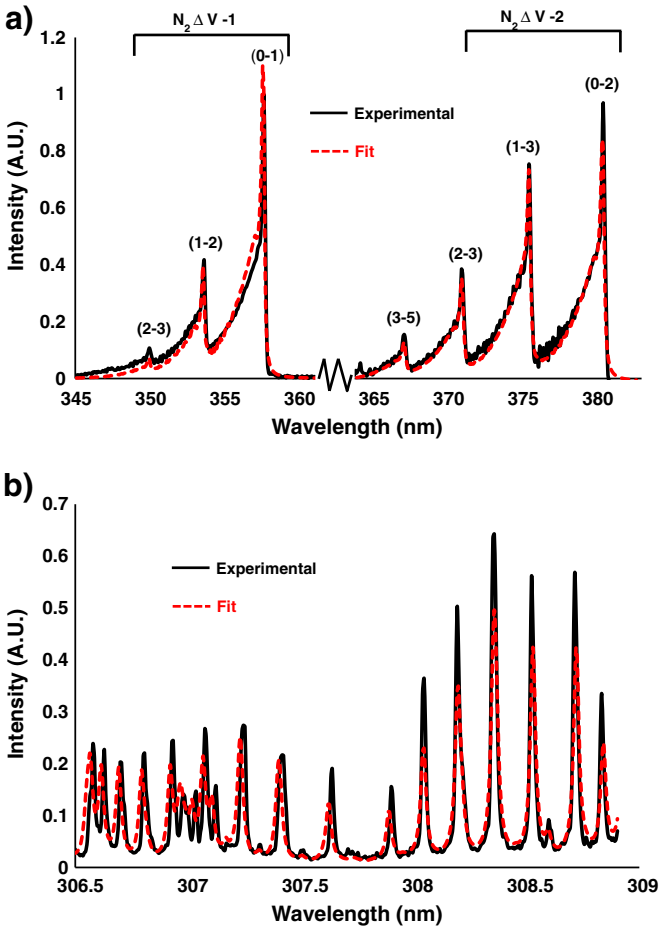

Fig. 2. Experimental fitting of the (a) N_2 second positive system ($c^3\prod_u \rightarrow B^3\prod_g$) and (b) OH $A_2\Sigma + (v = 0) \rightarrow X_2\Pi\ (v = 0)$ transition region.

effects of the three control parameters are displayed in the Pareto plot (Fig. 3b). The standardized effects, seen in Fig. 3b, reflect the fact that carrier gas flow rate (B) has the largest effect on rotational temperatures, that being a negative effect. In literal terms, increases in the He flow rate lower the kinetic temperature within the plasma region. This is not surprising as He has a very high thermal conductivity, effectively carrying kinetic energy from the plasma. As indicated by the vertical line in the plot, the other interactions have no statistical significance, though the magnitudes (positive and negative) provide insights into plasma processes.

In order to test for any perturbations in plasma energetics by sample loading, T_{rot} values were re-determined with the addition of the 1000 μg mL^{-1} Mg test solution. In this case, changes in T_{rot} are expected to reflect energetic loads due to the initial solution vaporization and droplet desolvation conditions. Introduction of Mg in the solution feed increased T_{rot} values by <100 K on average, which is within the experimental error. In the case of the LA-introduced Mg particles, one might expect a thermal load on the plasma for the vaporization of particles is more energy costly than creation of free atoms from solution. Here again, the average rotational temperature was not statistically different from the neat electrolyte solution. Importantly, the parametric response trends for the T_{rot} across the $n = 16$ combinations with sample introduction are essentially the same as projected in Fig. 3a and b.

The second spectrochemical probe for assessing T_{rot} is the OH band system. The high-resolution spectrometer was employed here due to the interference from the N_2 band ($\Delta v = 1$) seen in Fig. 1. A typical emission spectrum and corresponding fitting for the OH band is shown in Fig. 2b. The quality of the fittings are similar to those for N_2 above [10,37] using calculations [39] and constants [40] from the literature. The average T_{rot} across the $n = 16$ conditions was calculated to be 1311 K, with <1%RSD variability at any given set of conditions. While the temperatures derived for the two spectrochemical probes differ by ~500 K, the use of different spectrometers and detectors, and different levels of accuracy in the fitting and spectroscopic constants suggest that the values are in reasonable agreement.

Greater insight is revealed by evaluating the variation of OH T_{rot} as a function of the discharge parameters. While the response surface in Supplementary Data Fig. 1 is qualitatively similar to that of Fig. 3a, quantitatively it is seen that the OH-derived temperatures differ by a factor-of-2, while for the N_2-derived values differ by only ~40% as He flow rate is changed. This greater level of influence on T_{rot} is easily seen in the corresponding Pareto plot, as the standardized effect for He flow (factor B) has a value of ~23 *negative* in this case. Also seen in the OH-derived T_{rot}

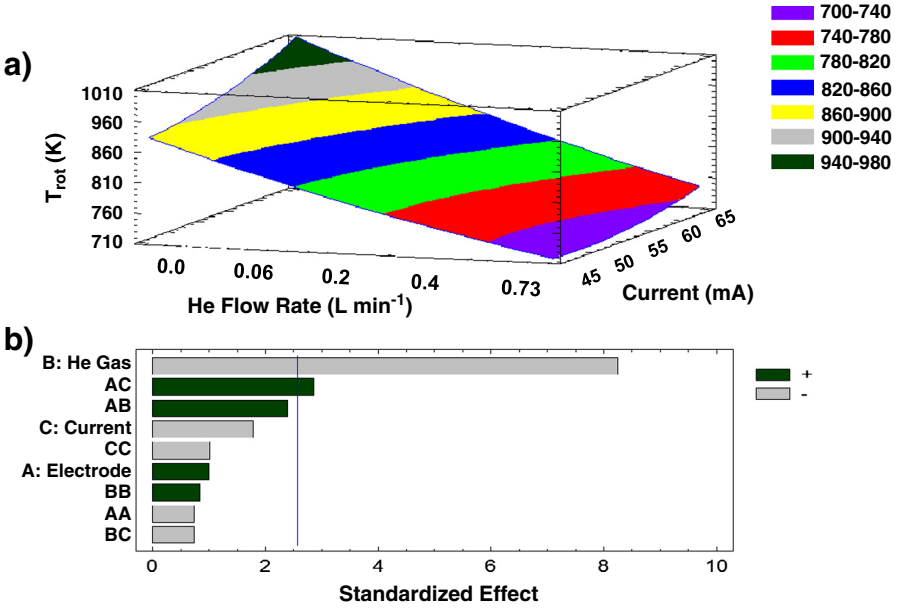

Fig. 3. a) Response surface for rotational temperatures determined by N_2 second positive system ($c^3\prod_u \rightarrow B^3\prod_g$) experimental fittings as a function of He flow rate and discharge current and b) Pareto plot illustrating parametric significance across the test parameter matrix.

trends, discharge current now has a significant positive effect with a quadratic positive effect also seen for gas flow rate (BB). The final significant effect is a negative quadratic effect of electrode spacing (CC). In general, the OH-derive T_{rot} values show greater parametric sensitivities than the N_2 values, but the directionality (positive or negative) is the same for each set of discharge parameters for both probe systems.

Rotational temperatures were accessed for the OH band emission relative the introduction of the Mg test solution and LA particles. Here it was also seen that the differences in the T_{rot} values (and their experimental variability) showed no statistical difference from the case of the neat electrolyte solution. This overall lack of perturbation of the gas kinetic temperatures implies that the power density within the microplasma (>10 W mm^{-3}) is sufficient in affecting the vaporization of solutions at a flow rate of 300 μL min^{-1} and the digestion of ns-LA particles. The extended residence times within the microplasma surely work to this end as well. The T_{rot} values reported here are typical of propane-air combustion flames [25] and low power atmospheric pressure plasmas [41,42]. They are lower as well in comparison to the SC-GD described by Hieftje and co-workers [43] and the miniaturized and dc-μAPGDs of Jamroz et al. [44,45].

3.3. Determination of excitation temperatures by He and Mg atomic lines

The excitation temperature (T_{exc}) is one of the central parameters for plasma characterization, describing the relative populations of atomic species in the ground and excited states under the assumption of a Boltzmann distribution. Many factors are incorporated into this type of distribution including statistical weights of specific levels, population density of the atom in the ground state, the atom's statistical weight, and excitation potential of the level [24,25,46]. As such, elements of very different atomic structure are prone to yield incongruent T_{exc} values, particularly in the absence of local thermodynamic equilibrium (LTE). To address this specific point, He I and Mg I transitions were used in this evaluation.

This work takes a similar approach used by Quintero to calculate T_{exc} from a high pressure microwave-induced plasma (MIP) [47], employing Boltzmann plots of four He I lines, using transition constants provided therein. While greater numbers of transitions is generally preferable, the correlation coefficients (R^2) for all of the derived Boltzmann plots (16 parameter combinations, each in triplicate) were all >0.900. The average T_{exc} values (for all parameters) calculated from the He I lines, was determined to be 2672 K, with temperatures ranging from ~2100–2900 K across the 16 different conditions. This ~3× increase between T_{rot} and T_{exc} is fairly common across the spectrum of spectrochemical devices, as the energy transfer between plasma electrons and atoms is more efficient than the heavy body collisions that distribute thermal energy. The response surface of Fig. 4a reflects the roles of He flow rate and discharge current on T_{exc} for a constant electrode gap value. The Pareto plot presented in Fig. 4b suggests that the He flow rate has a small positive correlation. While current and electrode distance individually have little effect, the combination of increasing the two (AC) does increase T_{exc} values to a small extent. This is an interesting relationship as increasing the electrode gap decreases the microplasma power density, while increases in current have the opposite effect. This cooperative effect will be discussed in a latter section pertaining to electron number density. Overall, the lack of significant effects suggests that the kinetic energy (temperature) of electrons in the plasma remains fairly constant across the parameters.

For comparison purposes, a set of four Mg I lines (from solution introduction) was used to calculate T_{exc}, yielding an average value of 2643 K. Fig. 5 illustrates the derived T_{exc} values for the 16 different plasma conditions calculated from both He I and Mg I lines. The He I transitions originate at excitation energies of ~23 eV, while those of Mg I involve relatively low energies of 4.3–5.1 eV. Under the simple assumption that conditions of LTE do not exist, very different values would have been expected [24,25]. The average values for these two probes are statistically the same, suggesting that the excitation environment/processes are very similar for these very different excited states. Introduction of Mg particulates via LA yielded an average T_{exc} value He I of 2564 K across the plasma parameter set, indicating that the particle load has no appreciable effect on the microplasma excitation conditions. Thus, a high level of robustness exists as heavy matrix solutions or LA particles of Mg are digested without perturbation of plasma excitation conditions.

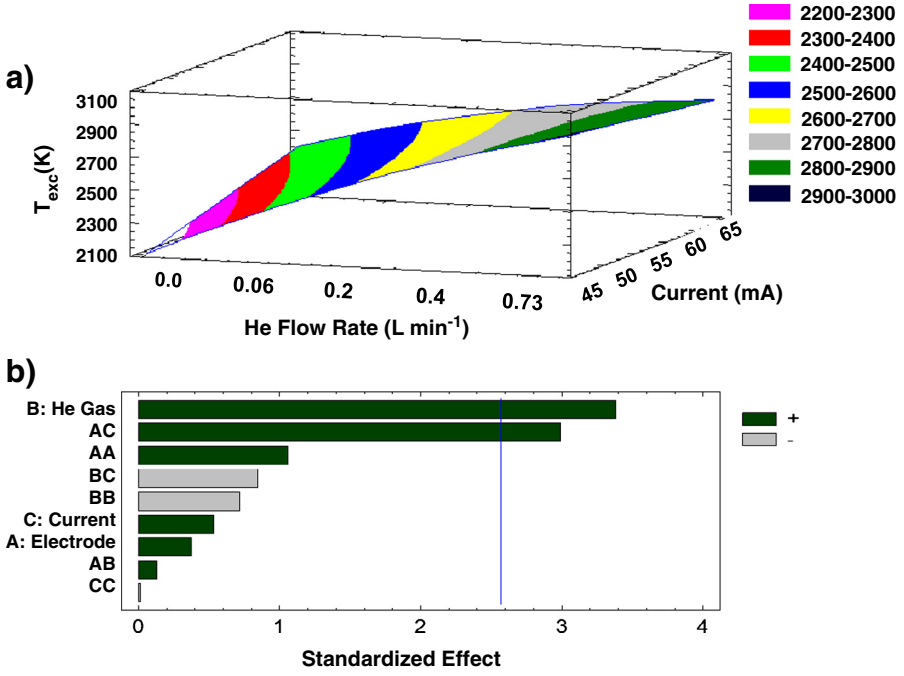

Fig. 4. a) Response surface for excitation temperatures determined by Boltzmann distribution of the He (I) lines as a function of He flow rate and discharge current and b) Pareto plot illustrating parametric significance across the test parameter matrix.

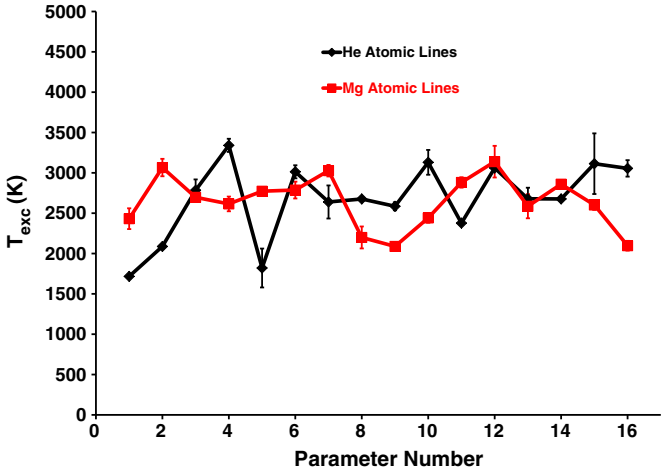

Fig. 5. Illustration of the two methods of calculating atomic excitation temperatures (He, Mg) and how they were related in regards to condition number.

3.4. Determination of electron number density by He and H line broadening

Previous works by Venzie and Marcus investigated potential matrix effects in the LS-APGD-OES source upon addition of EIEs [15]. The lack of any perturbations was attributed to a very high electron number density as milliamps of dc-current pass through the microplasma. The electron number density (n_e) is commonly determined through the Stark broadening of spectral lines emitted by argon (Ar), helium (He), and the hydrogen Balmer series (H_α and more commonly H_β) [21,22,35,46]. In the present work, two probes were employed to identify/circumvent potential biases. Firstly, the Balmer alpha line (H_α) was utilized for the calculation; however, instead of FWHM, the full width half area (FWHA) method was employed. Gigosos determined that when using FWHA, excitation temperatures play little role in effecting the number density and derived the equation for calculating n_e from the FWHA of the H_α line [48].

$$H_\alpha : \mathrm{FWHA} = 0.549\ \mathrm{nm} \times \left(\frac{n_e}{10^{23}\ \mathrm{m}^3}\right)^{0.67965}. \quad (1)$$

Based on this methodology, the average n_e was calculated to be 2.8×10^{15} cm^{-3} across the 16 plasma parameters. As seen in Fig. 6, the particular plasma parameters do not substantially change the derived number densities (with a range of 14%, relative) for the HNO_3 blank. Introduction of the 1000 μg mL^{-1} Mg^{2+} solution into the plasma has little effect on n_e, with the responses of the two solution types paralleling each other throughout the parametric matrix.

The second method for calculating n_e incorporated the He I 587.3 nm line, utilizing a different mathematical approach to limit potential bias. For this case, the FWHM was used for the Stark-broadened He line, with the electron impact parameter (W) required to complete this determination. The electron impact factor is a coefficient that is related to specific Stark broadened lines and specific excitation temperatures [49]. While it is temperature dependent, temperature plays an insignificant role in the determination and only loosely effects the calculation. Other parameters that play a role in obtaining Eq. (2) are the ion broadening parameter and population of particles in the Debye sphere.

$$\Delta\lambda_{\frac{1}{2}} = 2W \times \frac{n_e}{10^{16}}. \quad (2)$$

Based on the measured He I FWHM data, the average n_e was calculated to be 9.7×10^{15} cm^{-3} across the parameter space. While the magnitude of the number densities are on the same scale (~10^{15}), the He I-derived number density is ~3 times higher, which is likely due to the origins and concentrations of the two species in the microplasma environment. This increase could be due to pressure broadening of the He I line as the concentration of He species in and around the plasma is very high due to the flowing of He gas through both electrodes (0.2 L min^{-1} and ~0.5 L min^{-1}), and is reflected in Fig. 1 as He I intensities exceed those of H I. Self-absorption by He species in the cooler periphery

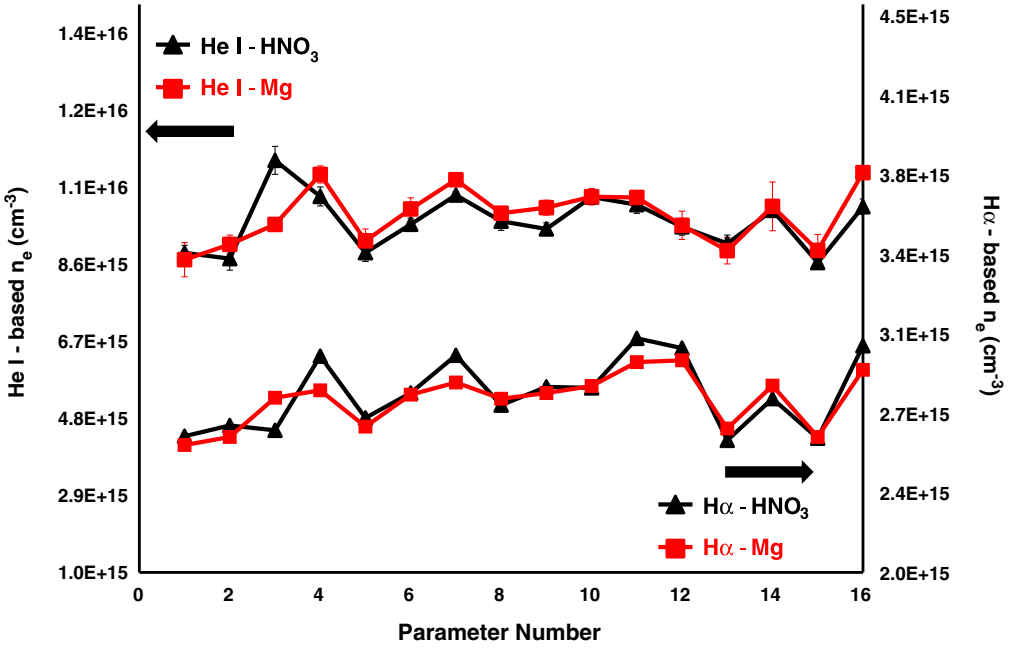

Fig. 6. Illustration of how electron number density was related to condition number with (red) and without (black) the introduction of Mg calculated from the H_α line (a) and the He 587 nm line (b). (For interpretation of the references to color in this figure legend, the reader is referred to the web version of this article.)

regions of the plasma would contribute to line broadening. Spatially-resolved measurements, likely with Abel inversion, will be needed to further evaluate this situation. Fig. 6 illustrates the same trends throughout the parametric evaluation with the He I-based n_e values, with and without the introduction of the Mg solution. In fact, the parametric dependencies seen in both means of calculating n_e parallel each other in the parameter space, serving to validate the two experimental approaches.

The spread of n_e values in Fig. 6 is not appreciable, though the response surface generated as a function of flow rate and discharge current, does show a slight n_e dependence on the carrier gas flow rate, as shown in Fig. 7a. The slight, but statistically significant, effect of carrier gas flow rates is borne out in the Pareto plot of Fig. 7b. Very interestingly, no other parameters, including the discharge current, have appreciable influences. The fact that n_e does not increase, even though the current is increased by a factor of 50% across the experiments, reflects the situation where the discharge volume is increasing; thus keeping the density relatively constant. By the same token, it is likely true that the counter flow of the He carrier gas may compress the plasma, thus increasing the density. This phenomenon would also explain the reasoning for the strong positive relationship between T_{exc} and gas flow rate.

3.5. Monitoring plasma robustness characteristics through Mg II:Mg I ratios

The Mg II:Mg I ratio is widely used to benchmark spectrochemical robustness and analytical performance of plasma emission sources. Typically this ionic:atomic ratio is monitored through changes in plasma conditions (parameter studies) or the introduction of other species that would potentially induce matrix effects [26,50–52]. There are essentially two aspects of the robustness parameter; the magnitude that reflects the ionization temperature (T_{ion}) of the source, and the measured value that one would want to be unchanged as conditions are changed (i.e., a robust plasma). In principle, any emitting ion:atom pair could be employed to assess changes in excitation/ionization conditions. The Mg (280.27 nm:285.21 nm) line pair is used here to allow comparisons with other sources and magnesium was easily introduced in the solution and particulate phases. Previous studies by Venzie and Marcus suggested an immunity to changes in the ratio with the addition of EIEs to the LS-APGD [15]. Fig. 8 illustrates the fact that both carrier gas flow rate and discharge current have minimal positive effects on the ratio. As might be expected from trends determined for T_{exc} and n_e, carrier gas is the parameter that affects the ratio to a larger extent. The magnitude of the ratio (ranging from 0.5 to 1.3) with an average of 0.7, suggests that the extent of forming excited stated Mg ions is low versus the ICP (ranging from 7–11 [26]). By the same token, the lack of large changes across the parametric matrix suggests that the LS-APGD should be relatively immune to fluctuations in excitation conditions due to minor imprecisions in operational control; an asset in field-based applications.

4. Conclusions

The liquid sampling-atmospheric pressure glow discharge (LS-APGD) has been characterized relative to its rotational (T_{rot}) and excitation (T_{exc}) temperatures, electron number densities (n_e) and robustness, with an eye towards applications as a secondary excitation source for LA particle analysis and field deployment applications. Carrier gas flow rate, electrode distance, and applied current were incorporated in the parametric overview in the cases of blank solutions (1% HNO_3), heavy solution matrices (1000 μg mL^{-1} Mg^{2+}), and Mg particles introduced via LA. The high power density (>10 W mm^{-3}) microplasma exhibits rotational and excitation temperatures that are in line with propane-air combustion flames and low power ICP and MIP sources. Excitation temperatures are on par with other glow discharge sources. On the other hand, the electron number densities were on par with analytical ICPs. In no case of sample loading (solution or LA particles) were there statistically significant changes in the determined plasma characteristics.

Further experimentation is needed in terms of introducing other solution matrices (composition and concentration) to generate a more in-depth profile of the susceptibility to analytical matrix effects. Understanding these plasma fundamentals allows the plasma to be modified for specific needs. Such fundamental studies will be extended to the recent demonstration of the LS-APGD as a source for ambient desorption ionization-mass spectrometry (ADI-MS) [53]. At this point, the analytical performance, low-overhead operational space, diversity in sample forms, and high levels of robustness of the microplasma suggest

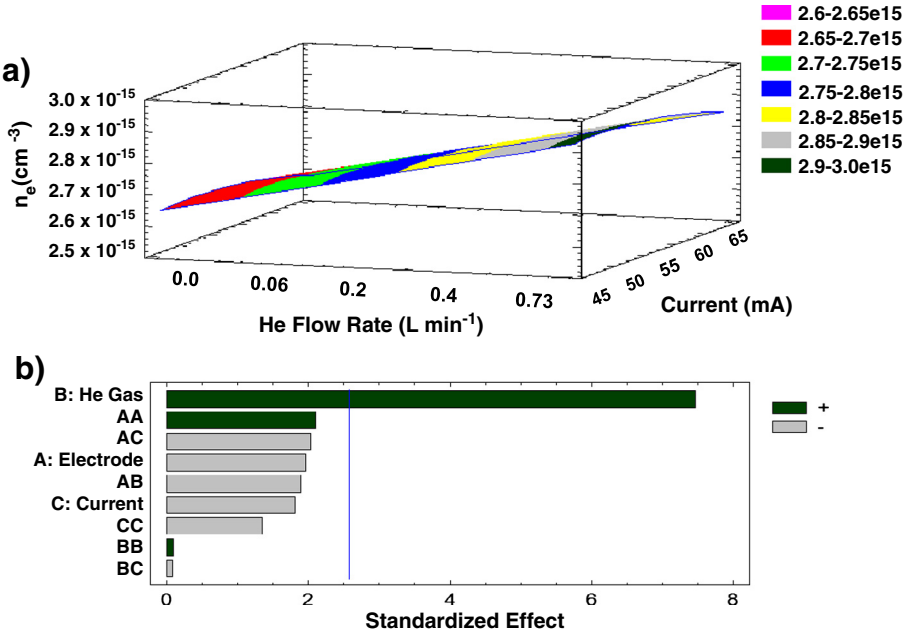

Fig. 7. a) Response surface for electron number densities determined by Stark broadening of the H_α line of the Balmer series as a function of He flow rate and discharge current and b) Pareto plot illustrating parametric significance across the test parameter matrix.

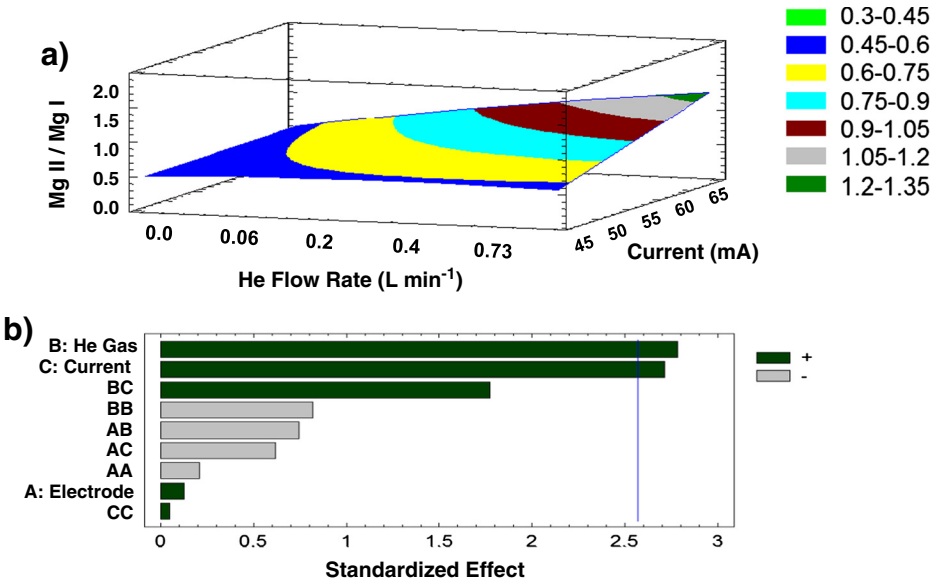

Fig. 8. a) Response surface for Mg II:I ratios as a function of He flow rate and discharge current and b) Pareto plot illustrating parametric significance across the test parameter matrix.

applications in areas where current laboratory-scale instrumentation is not appropriate.

Acknowledgments

Research was supported by the Separations and Analysis Program, Chemical Sciences, Biosciences, and Geosciences Division, Office of Basic Energy Sciences of the U.S. Department of Energy under contract number DE-AC02-05CH11231 at the Lawrence Berkeley National Laboratory.

Appendix A. Supplementary data

Supplementary data to this article can be found online at http://dx.doi.org/10.1016/j.sab.2014.03.004.

References

[1] N. Jakubowski, R. Dorka, E. Steers, A. Tempez, Trends in glow discharge spectroscopy, J. Anal. At. Spectrom. 22 (2007) 722–735.
[2] M. Webb, F. Andrade, G. Hieftje, Compact glow discharge for the elemental analysis of aqueous samples, Anal. Chem. 79 (2007) 7899–7905.
[3] P. Jamroz, K. Greda, P. Pohl, Development of direct-current, atmospheric-pressure, glow discharges generated in contact with flowing electrolyte solutions for elemental analysis by optical emission spectrometry, TrAC Trends Anal. Chem. 41 (2012) 105–121.
[4] K. Niemax, Laser ablation—reflections on a very complex technique for solid sampling, Fresenius J. Anal. Chem. 370 (2001) 332–340.
[5] R. Russo, X. Mao, H. Liu, J. Gonzalez, S. Mao, Laser ablation in analytical chemistry—a review, Talanta 57 (2002) 425–451.
[6] R.E. Russo, X. Mao, J.J. Gonzalex, V. Zorba, J. Yoo, Laser Ablation in Analytical Chemistry, American Chemical Society, Analytical Chemistry, 2013.
[7] J. Gonzalez, C. Liu, S. Wen, X. Mao, R. Russo, Metal particles produced by laser ablation for ICP-MS measurements, Talanta 73 (2007) 567–576.
[8] J. Gonzalez, C. Liu, S. Wen, X. Mao, R. Russo, Glass particles produced by laser ablation for ICP-MS measurements, Talanta 73 (2007) 577–582.
[9] F. Colao, R. Fantoni, V. Lazic, A. Paolini, F. Fabbri, G. Ori, L. Marinangeli, A. Baliva, Investigation of LIBS feasibility for in situ planetary exploration: an analysis on Martian rock analogues, Planet. Space Sci. 52 (2004) 117–123.
[10] M. Dong, X. Mao, J. Gonzalez, J. Lu, R. Russo, Time-resolved LIBS of atomic and molecular carbon from coal in air, argon and helium, J. Anal. At. Spectrom. 27 (2012) 2066–2075.
[11] J. Pedarnig, J. Heitz, E. Ionita, G. Dinescu, B. Praher, R. Viskup, Combination of RF-plasma jet and laser-induced plasma for breakdown spectroscopy analysis of complex materials, Appl. Surf. Sci. 257 (2011) 5452–5455.
[12] F. Pointurier, A. Hubert, A. Faure, P. Hemet, A. Pottin, Polyatomic interferences in plutonium determination in the femtogram range by double-focusing sector-field ICP-MS, J. Anal. At. Spectrom. 26 (2011) 1474–1480.
[13] J. Shelley, S. Ray, G. Hieftje, Laser ablation coupled to a flowing atmospheric pressure afterglow for ambient mass spectral imaging, Anal. Chem. 80 (2008) 8308–8313.
[14] W.C. Davis, R.K. Marcus, An atmospheric pressure glow discharge optical emission source for the direct sampling of liquid media, J. Anal. At. Spectrom. 16 (2001) 931–937.
[15] J.L. Venzie, R.K. Marcus, Effects of easily ionizable elements on the liquid sampling-atmospheric pressure glow discharge, Spectrochim. Acta Part B 61 (2006) 715–721.
[16] C. Quarles, B. Manard, C. Burdette, R. Marcus, Roles of electrode material and geometry in liquid sampling-atmospheric pressure glow discharge (LS-APGD) microplasma emission spectroscopy, Microchem. J. 105 (2012) 48–55.
[17] R.K. Marcus, C.D. Quarles, C.J. Barinaga, A.J. Carado, D.W. Koppenaal, Liquid sampling-atmospheric pressure glow discharge ionization source for elemental mass spectrometry, Anal. Chem. 83 (2011) 2425–2429.
[18] C.D. Quarles, A.J. Carado, C.J. Barinaga, D.W. Koppenaal, R.K. Marcus, Liquid sampling-atmospheric pressure glow discharge (LS-APGD) ionization source for elemental mass spectrometry: preliminary parametric evaluation and figures of merit, Anal. Bioanal. Chem. 402 (2012) 261–268.
[19] C. Quarles, J. Gonzalez, I. Choi, J. Ruiz, X. Mao, R. Marcus, R. Russo, Liquid sampling-atmospheric pressure glow discharge optical emission spectroscopy detection of laser ablation produced particles: a feasibility study, Spectrochim. Acta Part B 76 (2012) 190–196.
[20] A.J. Carado, C.D. Quarles, A.M. Duffin, C.J. Barinaga, R.E. Russo, R.K. Marcus, G.C. Eiden, D.W. Koppenaal, Femtosecond laser ablation particle introduction to a liquid sampling-atmospheric pressure glow discharge ionization source, J. Anal. At. Spectrom. 27 (2012) 385–389.
[21] G.M. Hieftje, Plasma diagnostic techniques for understanding and control, Spectrochim. Acta Part B 47 (1992) 3–25.
[22] J.M. Mermet, Spectroscopic diagnostics: basic concepts, in: P.W.J.M. Boumans (Ed.), Inductively-Coupled Plasma Emission Spectroscopy Part 2 — Applications and Fundamentals, John Wiley & Sons, New York, 1987, pp. 353–386.
[23] R. Mavrodineanu, H. Boiteux, Flame Spectroscopy, John Wiley and Sons, New York, 1965.
[24] P.W.J.M. Boumans, Theory of Spectrochemical Excitation, Hilger & Watts, Bristol, 1966.
[25] C.T.J. Alkemade, T. Hollander, W. Snelleman, P.J.T. Zeegers, Metal Vapours in Flames, Pergamon Press, Oxford, 1982.
[26] J. Mermet, Use of magnesium as a test element for inductively coupled plasma atomic emission-spectrometry diagnostics, Anal. Chim. Acta. 250 (1991) 85–94.
[27] J. Dennaud, A. Howes, E. Poussel, J.M. Mermet, Study of ionic-to-atomic line intensity ratios for two axial viewing-based inductively coupled plasma atomic emission spectrometers, Spectrochim. Acta Part B 56B (2001) 101–112.
[28] F. Iza, J. Hopwood, Rotational, vibrational, and excitation temperatures of a microwave-frequency microplasma, IEEE Trans. Plasma Sci. 32 (2004) 498–504.
[29] W.C. Davis, R.K. Marcus, Role of powering geometries and sheath gas composition on operation characteristics and the optical emission in the liquid sampling-atmospheric pressure glow discharge, Spectrochim. Acta Part B 57 (2002) 1473–1486.
[30] N. Konjevic, M. Ivkovic, N. Sakan, Hydrogen Balmer lines for low electron number density plasma diagnostics, Spectrochim. Acta Part B 76 (2012) 16–26.
[31] D.C. Montgomery, Design and Analysis of Experiments, 8th ed., 2001.
[32] P. Bock, Getting It RIght: R&D Methods for Science and Engineering, Academic Press, San Diego, 2001.
[33] R.K. Winge, V.A. Fassel, V.J. Peterson, M.A. Floyd, Inductively-Coupled Plasma-Atomic Emission Spectroscopy: An Atlas of Spectral Information, Elsevier, Amsterdam, 1985.
[34] G. Kornblum, L. Degalan, Spatial-distribution of temperature and number densities of electrons and atomic and ionic species in an inductively coupled RF argon plasma, Spectrochim. Acta Part B 32 (1977) 71–96.

[35] A. Monataser, D.W. Golightly, Inductively Coupled Plasmas in Analytical Atomic Spectrometry, VCH Publishers, Second ed., 1992
[36] S. Pellerin, J. Cormier, F. Richard, K. Musiol, J. Chapelle, A spectroscopic diagnostic method using UV OH band spectrum, J. Phys. D. Appl. Phys. 29 (1996) 726–739.
[37] M. Dong, X. Mao, J. Gonzalez, J. Lu, R. Russo, Carbon isotope separation and molecular formation in laser-induced plasmas by laser ablation molecular isotopic spectrometry, Anal. Chem. 85 (2013) 2899–2906.
[38] F. Roux, F. Michaud, M. Vervloet, High-resolution Fourier spectrometry of n-14(2) violet emission-spectrum—extensive analysis of the c-3-pi(u)-]b-3-pi(g) system, J. Mol. Spectrosc. 158 (1993) 270–277.
[39] E. Moore, W. Richards, Reanalysis of a2sigma-x2pi-i system of oh, Phys. Scr. 3 (1971) 223.
[40] M. NUSS, K. Gericke, F. Comes, Energy partitioning in the reaction o-16(1d) + (h20)-o-18-](oh)-o-16 + (oh)-o-18.6. The UV spectrum of (oh)-o-16 and (oh)-o-18, J. Quant. Spectrosc. Radiat. Transf. 27 (1982) 191–201.
[41] M. ABDALLAH, J. MERMET, Comparison of temperature-measurements in ICP and MIP with Ar and He as plasma gas, Spectrochim. Acta Part B 37 (1982) 391–397.
[42] J. Shelley, G. Chan, G. Hieftje, Understanding the flowing atmospheric-pressure afterglow (FAPA) ambient ionization source through optical means, J. Am. Soc. Mass Spectrom. 23 (2012) 407–417.
[43] M.R. Webb, F.J. Andrade, G. Gamez, R. McCrindle, G.M. Hieftje, Spectroscopic and electrical studies of a solution-cathode glow discharge, J. Anal. At. Spectrom. 20 (2005) 1218–1225.
[44] P. Jamroz, W. Zyrnicki, Spectroscopic characterization of miniaturized atmospheric-pressure DC glow discharge generated in contact with flowing small size liquid cathode, Plasma Chem. Plasma Process. 31 (2011) 681–696.
[45] P. Jamroz, W. Zyrnicki, P. Pohl, The effect of a miniature argon flow rate on the spectral characteristics of a direct current atmospheric pressure glow micro-discharge between an argon microjet and a small sized flowing liquid cathode, Spectrochim. Acta Part B 73 (2012) 26–34.
[46] P.W.J.M. Boumans, Inductively Coupled Plasma Emission Spectroscopy: Part 2, Wiley-Interscience, New York, 1987.
[47] M. Quintero, A. Rodero, M. Garcia, A. Sola, Determination of the excitation temperature in a nonthermodynamic-equilibrium high-pressure helium microwave plasma torch, Appl. Spectrosc. 51 (1997) 778–784.
[48] M. Gigosos, M. Gonzalez, V. Cardenoso, Computer simulated Balmer-alpha, -beta and -gamma Stark line profiles for non-equilibrium plasmas diagnostics, Spectrochim. Acta Part B 58 (2003) 1489–1504.
[49] H.R. Griem, Spectral Line Broadening by Plasmas, Academic, New York, 1974.
[50] G. Chan, W. Chan, X. Mao, R. Russo, Comparison of matrix effects in inductively coupled plasma using laser ablation and solution nebulization for dry and wet plasma conditions, Spectrochim. Acta Part B 56 (2001) 1375–1386.
[51] G. Chan, G. Hieftje, Investigation of plasma-related matrix effects in inductively coupled plasma-atomic emission spectrometry caused by matrices with low second ionization potentials—identification of the secondary factor, Spectrochim. Acta Part B 61 (2006) 642–659.
[52] G. Chan, W. Chan, X. Mao, R. Russo, Investigation of matrix effects in inductively coupled plasma-atomic emission spectroscopy using laser ablation and solution nebulization—effect of second ionization potential, Spectrochim. Acta Part B 56 (2001) 77–92.
[53] R.K. Marcus, C.Q. Burdette, B.T. Manard, L.X. Zhang, Ambient desorption/ionization mass spectrometry using a liquid sampling-atmospheric glow discharge (LS-APGD) ionization source, Anal. Bioanal. Chem. 405 (2013) 8171–8184.